Meteoritics & Planetary Science 39, Nr 2, 321–331 (2004)
Abstract available online at http://meteoritics.org

Mass-velocity distributions of fragments in oblique impact cratering on gypsum

Naomi ONOSE* and Akira FUJIWARA

The Institute of Space and Astronautical Science, Yoshinodai 3-1-1, Sagamihara, Kanagawa, 229–8510, Japan
*Corresponding author. E-mail: onose@planeta.sci.isas.ac.jp

(Received 20 July 2003; revision accepted 15 December 2003)

Abstract–Oblique impact cratering experiments into gypsum targets were performed, and masses and velocities of the fragments were measured within the observational limit of 0.1–100 m/s in velocity and 0.0003–1 g in mass. The fragments observed were divided in two groups according to ejection time: early fragments ejected conically within a few msec after the impact followed by late fragments consisting of hundreds of slow, small fragments ejected almost perpendicular to the target. The relationship between mass and velocity of early fragments was observed to follow a power law with an exponent of –0.11 ± 0.06, consistent with previous studies (e.g., Nakamura and Fujiwara 1991; Giblin et al. 1998). The cumulative number of fragments heavier or equal to a given mass versus fragment mass distributions shows a power law exponent of –1.49 ± 0.09 for late fragments and steeper than –0.49 ± 0.18 for early fragments. More than 10% of the mass was ejected from the crater with ejection speed slower than 2 m/s. Those fragments will reaccumulate on porous (<1500 kg/m^3) and small (<4 km in diameter) asteroids.

INTRODUCTION

The Hayabusa spacecraft (MUSES-C), launched in May 2003 by ISAS, Japan, will collect samples from the surface of a near-Earth asteroid of <1 km diameter and bring them back to the Earth (Yano et al. 2002). The amount of the material collected greatly depends on the state of asteroid's surface. It is especially important to know whether or not a regolith exists on such a small body.

The NEAR-Shoemaker spacecraft provided high-resolution images of 433 Eros showing regolith consisting of cm-sized particles (Yeomans et al. 2000; Chapman et al. 2002). Meanwhile, Veverka et al. (1986) showed that rocky asteroids smaller than 20 km in diameter should lose almost all of their ejecta. Asteroids of such small diameter have very small self-gravity, and they had previously been thought to have little regolith on them. Impact cratering on asteroidal surfaces produces a lot of fragments. However, most of them are believed to escape from small asteroids.

The mismatch between observations and conventional theory may be explained with three reasons. First, previous studies of fragment velocity produced by impact cratering on cohesive bodies have been focusing mainly on the faster fragments (e.g., Gault et al. 1963; Gault and Heitowit 1963; Polansky and Ahrens 1990; Love et al. 1993; Shrine et al. 2002). The experimental procedures used in those studies were not suitable to detect the slower fragments from the interior of the target. Second, in those studies, the number of fragments measured in each run was too small. A few tens of fragments cannot represent the entire ejecta from an impact cratering. And third, extrapolation to the low velocity region (slower than 10 m/s) of a power law obtained through curve fitting for fragment velocity-cumulative mass distributions of the fragments ejected faster than a given velocity is potentially risky.

Porosity is one important factor to be considered. New data from observations of asteroid mutual perturbation events and spacecraft encounters have indicated that most asteroids have bulk densities smaller than the grain density of meteorites (Britt et al. 2002). Therefore, it is important to study the outcome of impact on porous media. Love et al. (1993) produced impact cratering experiments on porous media and indicated that they produce slower fragments than those on dense targets.

To investigate the production of collisional regolith on a low density and small body, impact cratering experiments on porous bodies stressing on slower ejecta are required. The mass and velocity of the fragments were measured using three high-speed video cameras. We used gypsum as the porous targets. Although gypsum may not be so similar to the asteroid material, using this material has the great advantage of understanding the fundamental process and outcomes of cratering on porous media. For example, it has high porosity (64% in this study) and enough uniformity (diameter of pore is about 0.3 mm) to investigate the effect of high-porosity on impact cratering. Pores of gypsum target can be evacuated since they have an open pore structure. The color is white, which is convenient for getting a clear image of the fragment even under insufficient exposure conditions accompanied with the high framing rate. They are shaped easily and are also inexpensive. Furthermore, less porous gypsum targets potentially will be obtained by forcing water out of the mold under pressure, immediately after casting (Vekinis et al. 1993). Effects of oblique incidence were also investigated, for impacts on planetary bodies are typically oblique.

EXPERIMENTAL PROCEDURE

Gypsum with density of 840 kg/m^3 was chosen as an analogue for porous asteroids. The $CaSO_4 \cdot ½H_2O$ starting powder was mixed with water in the ratio of 10:9 and was cast into split rectangular molds and allowed to cure for at least 20 days. Then, interlocking needle shaped gypsum crystals ($CaSO_4 \cdot 2H_2O$) construct a coherent mass. Since the true densities of the hemihydrate and dihydrate are about 2750 and 2320 kg/m^3, respectively, the porosity of the target employed in these experiments is estimated to be about 64%. The acoustic longitudinal wave velocity of this sample is 2200 m/s, and the Hugoniot equation of gypsum is given in Simakov et al. (1974) as $w = 2.45 + 1.80\ u$. The tensile strength of this target is extrapolated from Vekinis et al. (1993) to be ~1 MPa.

Targets of various sizes were prepared for various impact angles ranging from a 90 × 90 × 40 mm parallelepiped to a 400 × 362 × 260 mm hexagonal pillar to avoid the side surfaces chipping off because of the impact.

A two-stage light gas gun was used to accelerate nylon sphere projectiles 7 mm in diameter and 0.21 g in weight to about 4.2 ± 0.3 km/s. The incident angles, measured from the vertical, were 0° (vertical), 45°, 60°, and 70°. Two chambers and two gas strippers were inserted between the barrel and an evacuated steel target chamber of about 50 cm in diameter with side and top windows to avoid the dynamic disturbance due to propellant gas. The ambient pressure in the target chamber before impact was less than 200 Pa, and the distance between the muzzle and target was about 5.5 m.

Figure 1 shows the setting in the target chamber, including the definition of impact angle. The interior of the target chamber was lined with a 10 mm-thick layer of sponge plus cloth to avoid secondary fragmentations and rebound of the fragments. A target box with a slit 15 mm wide was employed in some experiments to focus on a cross section of the ejecta flow. By using the slit, the fragments' trajectories were limited in a plane including the projectile trajectory and were perpendicular to the target surface. As shown in Fig. 1a, lateral surfaces were impacted to observe slow fragments in vertical impacts, though fragments slower than 1 m/s that originated from the bottom of the crater (point A in Fig. 1a) would not be able to come out from the slit due to the gravity of the Earth. In some oblique impacts, the impacted surface of the target was oriented downward to allow the slowest fragments to fall from the crater and be observed without disturbance.

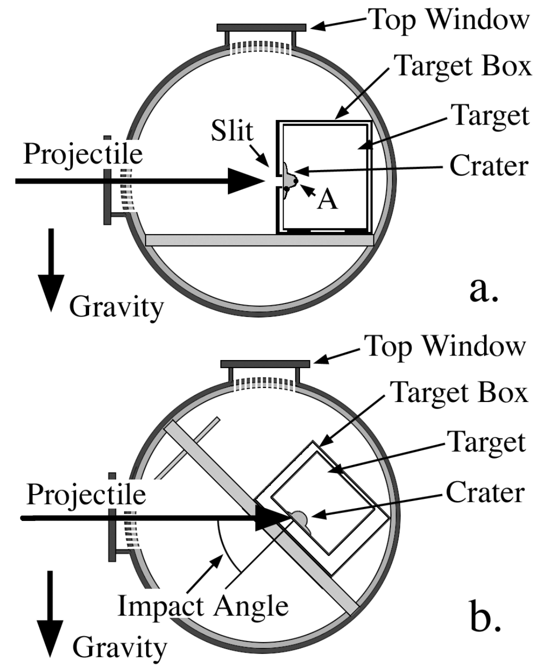

Fig. 1. Side view sketch of the experimental set up. A target box with a slit was used. The opening of the slit was 15 mm wide, and the slit was in the same plane of the projectile trajectory, perpendicular to the target surface: a) a setting for a vertical impact (experimental run No. 12). We shot lateral surfaces of the target, and the cratering process was filmed through a top window. A fragment originating at the bottom of a crater (point A) and having ejection velocity smaller than 1 m/s will not be able to come out from the slit. CCD pictures are taken from the top window for this experiment; b) a setting for a 45° impact angle (experimental run No. 16). The target face was downward, and CCD-pictures were taken from the side window.

Two high-speed 16 mm film cameras and a high-speed CCD video camera were used to observe the fragments in flight. The framing rates of the cameras ranged from 3000 to 9000 frames/sec. Some experiments employed two cameras to get the 3D velocity of the fragments. The experimental conditions are listed in Table 1.

ANALYSIS

Figure 2 shows some sample frames from the high-speed CCD video camera. They have resolutions of 255 × 255 and 126 × 255 pixels, with framing rates of 4500 and 9000 frames/sec, respectively. The pictures of the 16 mm high-speed film camera were scanned with a resolution of 1350 dpi, which is comparable to the grain size of the film. Each fragment in each frame was tracked and outlined. The positions and sizes of the fragments silhouettes were measured where the position was defined by the center of the projected area of the fragment image. From the trajectory of each fragments' two-dimensional projected velocity,

Table 1. Experimental conditions.

Run	Impact			Target	High-speed cameras			Minimum	Number of fragments			Shot	
	Velocity	Angle	Energy	mass	Framing rate								
no.	(km/s)	(deg.)	(J)	(kg)	(frame/sec)		Window	mass (g)	All	Earlier	Later	surface	Remarks
01	4[a]	70	1680	0.847	CCD	4500	side	0.0015	128	64	64	upper	2D[b]
10	4.27	0	1960	5.125	CCD	4500	side	0.0006	555	162	393	side	2D[c]
12	4[a]	0	1728	4.996	CCD	4500	top	0.0003	810	73	737	side	3D
14	4.31	60	2006	1.318	CCD	4500	side	0.0003	303	101	202	lower	2D
15	4.36	45	2034	2.471	CCD	4500	top	n.a.	47	47	n.a.	side	2D[c, d]
16	4[a]	45	1720	2.542	CCD	4500	side	0.0015	349	107	242	lower	3D[e]
52	4.08	70	1747	0.872	CCD	9000	top	n.a.	13	13	n.a.	side	2D[c]
93	4.37	70	2030	0.803	CCD	9000	side	n.a.	7	7	n.a.	upper	2D[c]
131	3.7	45	1437	2.08	16 mm	3000	top	n.a.	15	15	n.a.	side	2D[c]
					CCD	9000	side	n.a.	21	21	n.a.	side	2D
291	4[a]	0	1680	7.166	16 mm × 2	3000	both	n.a.	37	36	1	side	3D, 2D[c]

[a]The setting of the light-gas gun was for the impact velocity of 4 km/s, but velocity of a projectile could not measured.
[b]Slower fragments were not detected with this setting.
[c]Analysis were done only for ealier or larger fragments.
[d]An observational area was limited to up-range half.
[e]The slowest fragments were ignored for the disturbance from secondary collision in the target box became too large.

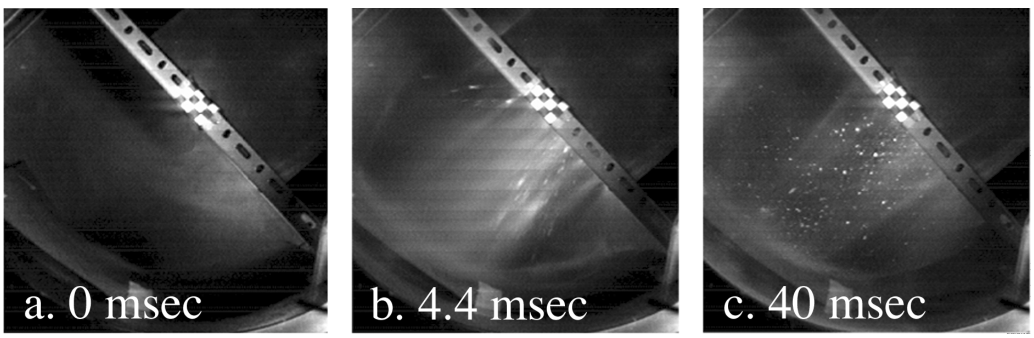

Fig. 2. Selected frames from the high-speed CCD video camera for experiment No. 16. The setting of the chamber is the same as in Fig 1a. The time after the impact is shown in msec: a) before impact; b) early fragments were ejected conically; c) late fragments were ejected perpendicular to the target surface.

projected initial position, and ejection time (defined as the time when the fragment leaves the target surface level) were obtained. The fragments that seem to undergo secondary collisions were excluded.

The detectable velocity and diameter ranges of the fragments were ~0.1–100 m/s and 1–50 mm, respectively. Fragments faster than this range could not be measured due to a combination of the slow framing ratio and an early powdery impact ejecta cloud, while fragments slower than 0.1 m/s are very sensitive to disturbances such as projectile accelerating gas, the impact produced vapor, and ejecta from secondary fragmentations of the faster fragments. In vertical impacts, the observed slowest ejecta from the bottom of the crater are estimated geometrically to be 0.5 m/s and 1 m/s, for experiments with and without using a slit, respectively (see Fig. 1a). The smallest fragment sizes correspond to the resolution of the high-speed camera and are approximated by a knee at the smallest range in the mass-cumulative number distributions (see discussion below). The number of fragments measured on the film is listed in Table 1.

For some experiments, only two-dimensional (2D) velocities were determined due to difficulties of identifying the same fragment on different films. The error accompanied with using 2D velocity instead of 3D velocity was no more than 50% because most fragments in this velocity range were ejected at an elevation angle of 60°.

The three-dimensional (3D) velocity was derived by three different methods:

a) using two pictures taken from two different directions. For run No. 291, where both top-view and side-view pictures were taken, some of the fragments in the top-view film could be identified as the same fragments seen in the side-view film. In this case, the estimated velocity error was 4%;
b) observation of fragments ejected through a slit. In runs No. 12 and No. 16, a target box with a slit enabled us to see the cross sectional view of the ejecta flow. The velocity components parallel to the optical axis of the high-speed camera can be neglected. The thickness of the slice through which the ejecta flew was 15 mm at the slit, and it gradually increased as the distance from the slit increased. The velocity error is estimated to be 20%

at most. Employing the slit results in an additional advantage of clear visualization of the fragments by reducing both the number and the overlapping trajectories of the fragments. On the other hand, the experiments using the slit suffer from the disadvantage of disturbances. A few tens of fragments larger than 4 mm in diameter may collide with the slit, and remain in the target box. Furthermore, in the final stage of ejection, the interaction of the ejecta flow with the slit plate makes the observation of the slowest fragments difficult;

c) secondary impacts on the window of the target chamber. Secondary impacts on the window of the target chamber occurred for experiments that did not make use of the target box. Estimating the initial position and ejection time to be the impact point and impact time, respectively, 3D velocity of the fragments was derived. The velocity error associated with this procedure is thought to be less than 20%. In this case, it was not possible to estimate the fragment mass because the secondary collision caused refragmentation. If the fragment collided with the window after some tracking, it was possible to obtain both fragment mass and 3D velocity from the images.

In each run, all fragments were collected. Fragments larger than 4 mm were numbered, weighed, measured, and remapped to the original target as much as possible to obtain the original positions of the fragments and to compare with images of the fragments on the film. The recovered fragments were measured to 0.01 g, and fragments heavier than about 0.1 g were identified with fragments on the film. Roughly 10 fragments were identified in each vertical impact experiment, including a few fragments smaller than 0.1 g.

Fragment diameters were estimated by assuming a spherical shape for the fragments. For each fragment, the average silhouette size was determined by combining those of all the frames, and it was converted into fragment radius by fitting the fragment silhouette to a circle. The fragment mass was then estimated by multiplying its volume by the target density (840 kg/m^3).

However, as shown in Fujiwara et al. (1978), the impact-produced fragments are not spheres, so a shape factor should be introduced in our calculations. For the fragments identified, the mass M_R (g) measured after recovery is empirically related to the estimated fragment mass M_E (g) as:

$$M_R = 0.37 \pm 0.02\, M_E \tag{1}$$

from curve fitting of the experimental data of runs No. 10 and No. 291.

For imaged fragments that could not be paired with a recovered fragment, each fragment mass was estimated from the average fragment silhouette by using Equation 1. The shape of the fragments was assumed to be size independent. The main uncertainty in fragment mass is due to the rotation of individual fragments, and it is estimated to be 50% at most. The insufficient quality of the image and the camera-to-fragment distance are also to be considered as possible causes of the error.

RESULTS

Mass-Velocity Relation in Vertical Impacts

Fragments were classified into two groups according to their ejection times. The group observed immediately after the initial ejection of fine and fast fragments (jetting) contains fragments ejected early. The other group contains fragments ejected late. These two groups represent two aspects of ejecta flow, changing with time. As seen in Fig. 2, fragments were ejected conically in the early phase (Fig. 2b), while almost vertical to the target surface in the late phase (Fig. 2c), as suspected in Gault and Heitowit (1963).

The relation between ejection time and ejection angle is shown in Fig. 3a for a vertical impact experiment performed with a target box and slit. An ejection angle of 90° means a trajectory normal to the target surface, while 0° and 180° correspond to trajectories parallel to the target surface. The errors in ejection angle are <5°, while the uncertainties in ejection time are estimated to be 1 msec for fragments ejected faster than 6 m/s, 10% for those between 1 and 6 m/s, and 50% for those below 1 m/s.

Figure 3b shows average ejection angles and their standard deviations for each ejection time bin. An ejection angle of fragments ejected earlier than 2 msec is 66°, while the fragments ejected between 10 and 15 msec are concentrated within 75° and 90°. Fragments ejected later than

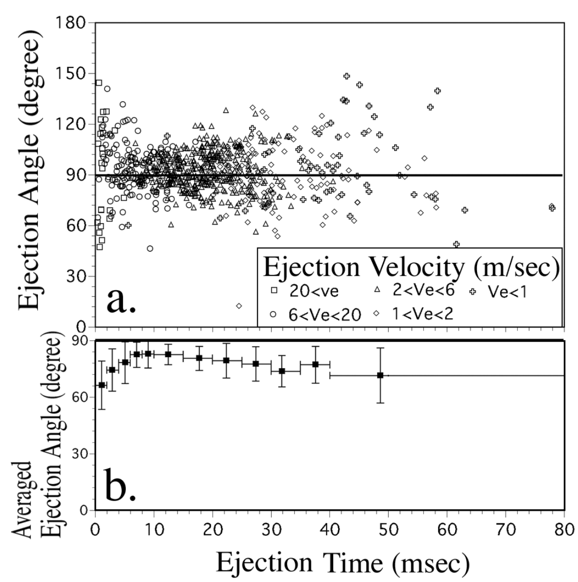

Fig. 3. a) Ejection angle and ejection time for the 0° (vertical) impact angle. In this experimental run (12), a target box with a slit enables us to obtain 3D velocity of the fragments. The legends indicate velocity bins; b) averaged ejection angles and their standard deviations for each ejection time bin.

30 msec show a large dispersion, implying the influence of secondary collisions within the fragments.

First, faster, and earlier fragments were ejected conically between 40° and 70° from the target surface. After a few msec of conical flow, the late, slower fragments were ejected almost vertically to the target surface and gradually diverge both in ejection angle and ejection time. The beginning of the late ejection seems to occur around 5 msec, when the number of fragments ejected between 80° and 90° starts to increase rapidly. We find that, out of 809 fragments identified, 737 were ejected later than 5 msec in experiment No. 12. Later ejection times imply that these fragments come from deep inside the crater. Note that the accuracy of the ejection time data for the late fragments is lower than that of earlier fragments, and the presence of the slit reduces the number of fragments ejected. Although the early and late fragments groups overlap between about 4 and 8 msec, it is appropriate to define early and late fragments as those ejected earlier and later than 5 msec, respectively, for vertical impacts. Fragment velocity decreases as the ejection time increases.

Figure 4 shows the relation between ejection velocity and fragment mass for three vertical impacts combined. Data from experiment No. 12 were supplemented with two additional experimental runs because the slit in experiment No. 12 prevents the observation of larger fragments. In experiments No. 10 and No. 291, only large or fast fragments were checked and tracked. The number of data points for experiments No. 10 and No. 291 are 30 and 36, respectively.

More than 90% of late fragments have velocity and mass between 0.86 to 8.6 m/s and 0.0002 to 0.0016 g, respectively. Some ejected fragments are slower than 0.8 m/s, and a small

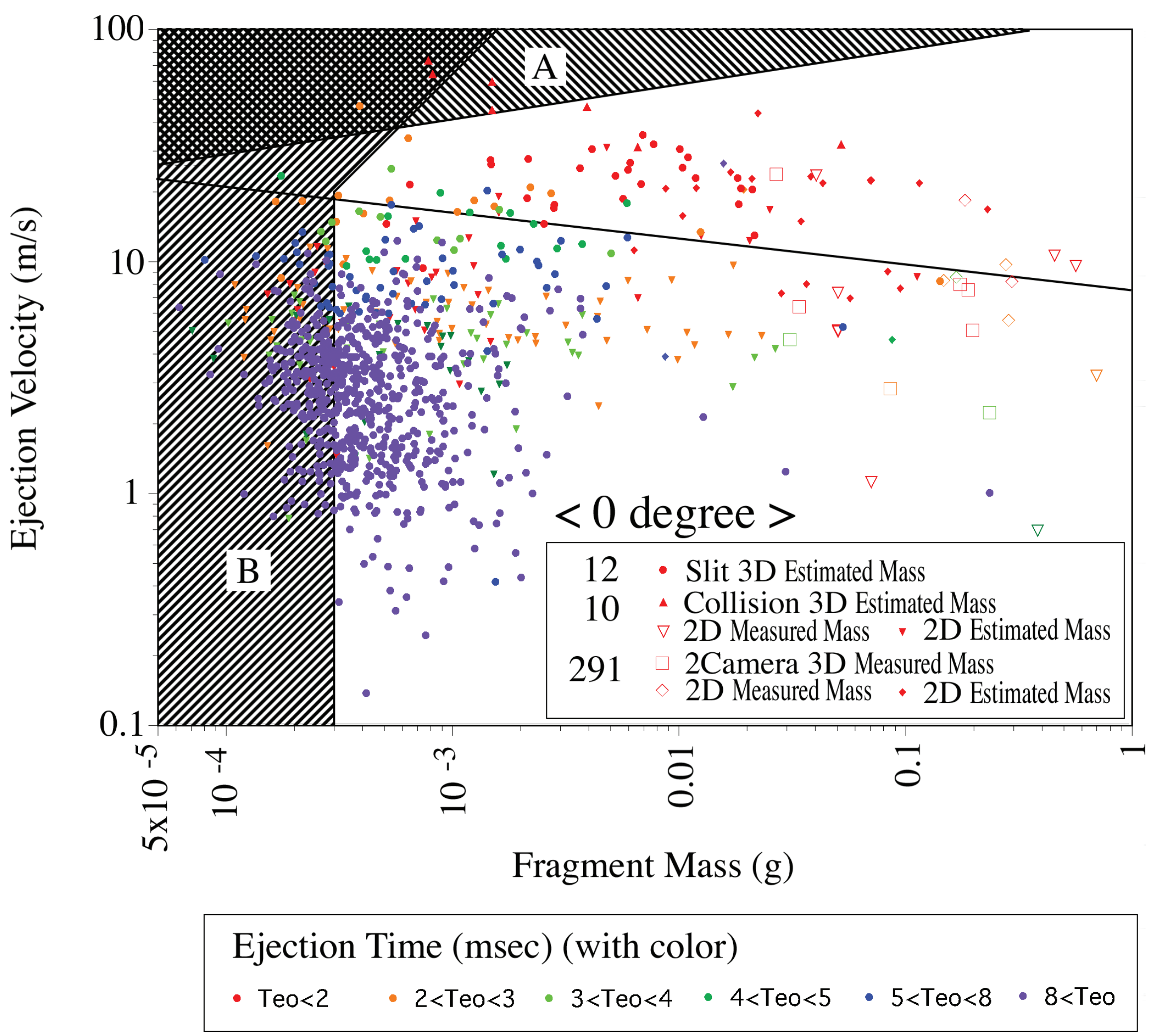

Fig. 4. Fragment mass versus two-dimensional (2D) and three-dimensional (3D) velocity for three vertical impacts (experiments No. 12, No. 10, and No. 291). The colors indicate different ejection times after impact, estimated from the trajectory of each fragment. The shapes represent various experiments and different ways to get fragments' masses. The hatched areas (A) and (B) represent regions where measurements are difficult to obtain because the fragments are either too small or too fast, respectively. The solid line shows the fit to the fragments ejected earlier than 5 msec.

number of ejected fragments are slower than the geometrical observation limit of 0.5 m/s (see Fig. 1), so they may originate in the shallower part of the crater or may collide with slits and get reflected. This late group of fragments consists of many slow and small fragments, which are also mentioned but not measured in Nakamura and Fujiwara (1991). The fact that 80% of them were ejected within 12.2 mm of the impact point means that they started from the interior of the bowl shaped region of the crater.

For fragments ejected earlier than 5 msec, a power-law relationship between fragment velocity (V) and mass (m) was suggested. Laboratory disruption experiments (Nakamura and Fujiwara 1991; Nakamura et al. 1992) have suggested this general power-law of the form:

$$V \propto m^k \tag{2}$$

The value of k fitted to early fragments is -0.11 ± 0.06, and it is consistent with the result in Nakamura and Fujiwara (1991), which deals with fragments originating from the surface of the target.

Larger fragments are mainly ejected by spallation, the separation of large fragments from a free surface as a result of dynamic tensile failure. In vertical impacts, two layers of spall fragments have been observed, a first spall layer, which includes the original surface of the target, and a second spall layer from the interior of the target. The second spall layer of fragments was ejected after the spall fragments from the top layer were ejected and had a slower velocity than the first spall layer. This second spall layer, with total weight of 0.44 g, was tracked and measured in these experiments, though the fragments' velocity was too small to extract ejection time.

Mass-Velocity Distributions in Oblique Impacts

For impacts with oblique incidence, the ejection angle versus ejection time is shown in Fig. 5. Experimental conditions for the oblique impacts are a little different from the vertical ones. For the 45° impact (No. 16), the target box was employed and the slit was set 50 mm from the target surface. The latest fragments were not observed due to the secondary collisions in the target box. The target box with the slit was not used in the 60° and 70° impacts (No. 14 and No. 01, respectively). And since the upper surface was shot in the 70° impact, most of the late fragments were not observed. As for the vertical case, the downrange and uprange directions are expressed by 0° and 180°, respectively. For the impact at 0° (vertical impacts), the later half of the diagram (Fig. 3) is not shown here to maintain the same ejection time axis as for the oblique impacts, in which the ejection sequence ends earlier than in vertical impacts.

In oblique impacts, earlier fragments are ejected conically as in vertical impacts, but the onset of the late ejection seems to be earlier than in the vertical cases. In 45° impact experiments, the onset of late ejection occurs sooner

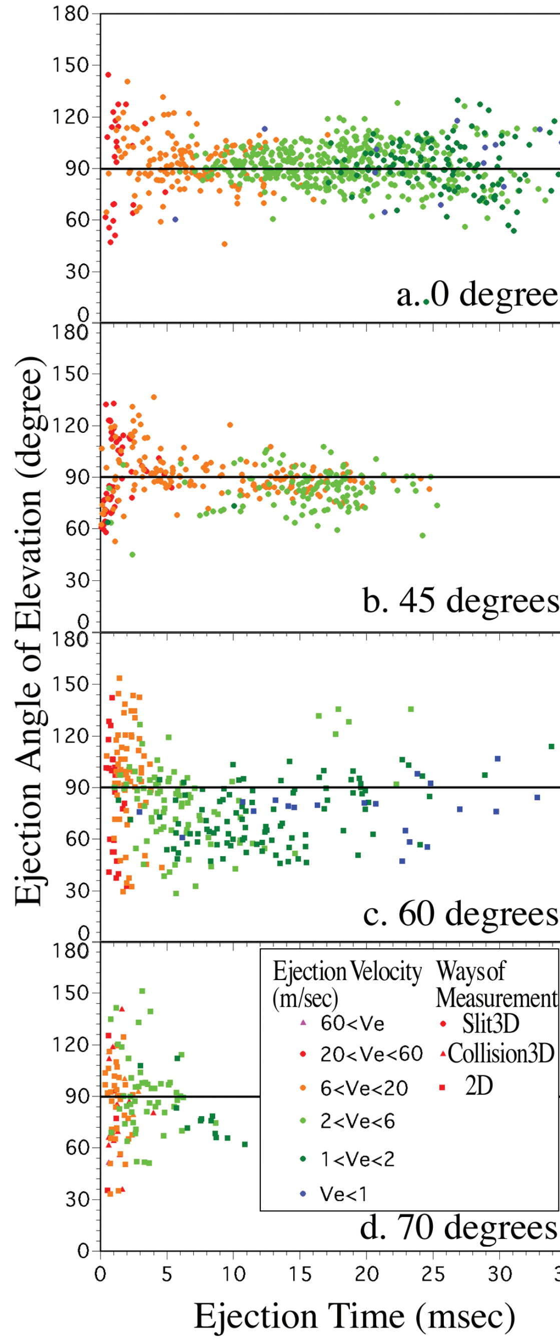

Fig. 5. Ejection angle versus ejection time. In the ordinate, 0°, 90°, and 180° represent the downrange, right upward, and uprange directions, respectively. The shapes represent different methods used to obtain velocity. Circles and triangles indicate 3D velocities of fragments obtained by use of slits and secondary collisions on the window, respectively. The squares represent 2D projective velocities of the fragments. The colors represent different ejection velocity bins: a) 0° impact angle experiment, employing the target box with the slit. The second half of the data was cut to keep the same abscissas range as the figure for the oblique impacts; b) 45° impact angle experiment, employing the target box with the slit. The latest fragments were not observed due to secondary collisions in the target box; c) 60° impact angle experiments, without use of the target box; d) 70° impact angle experiment, without target box. In this experiment, the impacts occur on the upper surface of the target.

Table 2. Summary of velocity data.

Impact angle (degree)	Later ejection begins at (msec)	Slope of mass velocity distributions for earlier fragments	Average ejection angle of elevation (degree)	
			Earlier	Later
0	5	–0.11	94.1	91.9
45	4	–0.068	91.6	86.3
60	3	0.15	91.4	75.7
70	2	–0.072	82.7	84.5

than in the case of a 0° impact from Fig. 5. It seems that this transition occurs even earlier in the 60° and 70° impacts, though the transitions from early to late ejection in the oblique impacts become progressively more obscure as the impact angle increases. The onset of the late ejection for oblique impacts are listed in Table 2. As the impact angle increases, the total number of fragments decreases.

The average ejection angle of late fragments tends to lean downrange with increasing impact angle, though they diverge further than the vertical impact cases. Figure 6 shows the 2D average direction for each group of fragments. Average angle was not calculated in the 70° impact angle because it was not possible to determine a clear boundary between early and late fragments. The average ejection angle for late populations was 76° from the target surface in the 60° impact. Ejection angles of early fragments also seem to decrease with increasing impact angle, but they showed no significant differences from normal ejection with a level of significance of 0.05.

The mass-velocity distributions for the fragments produced in oblique impacts are shown in Fig. 7. In experiment No. 16, only a small number of large fragments were observed because the slit prevents the larger fragments from going through. Data from experiment No. 16 were supplemented by two more experimental runs, No. 15 and No. 131. Data from two more experimental runs are added to the 70° impact experiment because the number of large fragments decreases suddenly above a 60° impact angle. Although the fastest fragment in each experiment appears to have practically the same value, irrespective of impact angle, the number of fast fragments decreases with increasing impact angle. The number of fragments slower than 0.8 m/s was small, even for the impact at 60°, without the slit, when shooting the lower surface of the target.

The value of k in Equation 2, fitted to early fragments, is about –0.07 for fragments ejected after 4 msec and 2 msec in 45° and 70° impacts, respectively. The slope of the impact angle at 60° is higher, and it may be because of the lack of larger fragments. However, the numbers of data for oblique impacts are not enough, since oblique impacts produce smaller numbers of fragments than vertical ones. Large fragments investigated in this study were mainly spall fragments, and as the impact angle increases, the amount and size of the spall fragments decreases. Errors may also arise from the overlapping of the two groups. The indices of mass-velocity distributions are shown in Table 2.

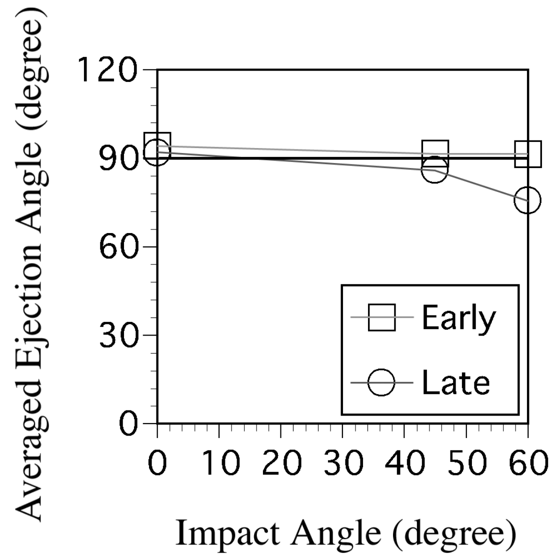

Fig. 6. Average ejection angle versus impact angle. Data from the 70° impact angle experiment are not shown here. Standard errors are similar to the shape sizes.

Mass-Cumulative Number Distributions

The cumulative number of fragments larger than or equal to a given mass versus fragment mass is shown in Fig. 8 for each impact angle: 0° (8a and 8b), 45° (8c), and 60° (8d). Data for the 70° experiments are not shown here because the experimental conditions for this run prevent us from observing the later fragments. A weighed mass was used for recovered fragments that were identified in the film. For the other fragments, we used the mass estimated from their silhouette sizes. In runs No. 291 (0°) and No. 15 (45°), only the fragments belonging to the early population were analyzed. Data from the four experiments (experimental runs No. 10, No. 12, No. 14, and No. 16), including oblique ones, are divided into early and late fragment groups. The graphs show a flat region in the smallest fragment mass region displaying the detectable lower limits in the fragment masses. These detectable limits are shown in Table 1 for each run, and they correspond to two pixels in the original video frame. Detection efficiency decreases significantly in the region where the fragment mass is smaller than this detection limit. The largest fragment means the largest fragment ejected from the crater cavity and not the original target within a crater.

Takagi et al. (1984) divided the mass distribution of basalt into three regions by two inflections in almost the same

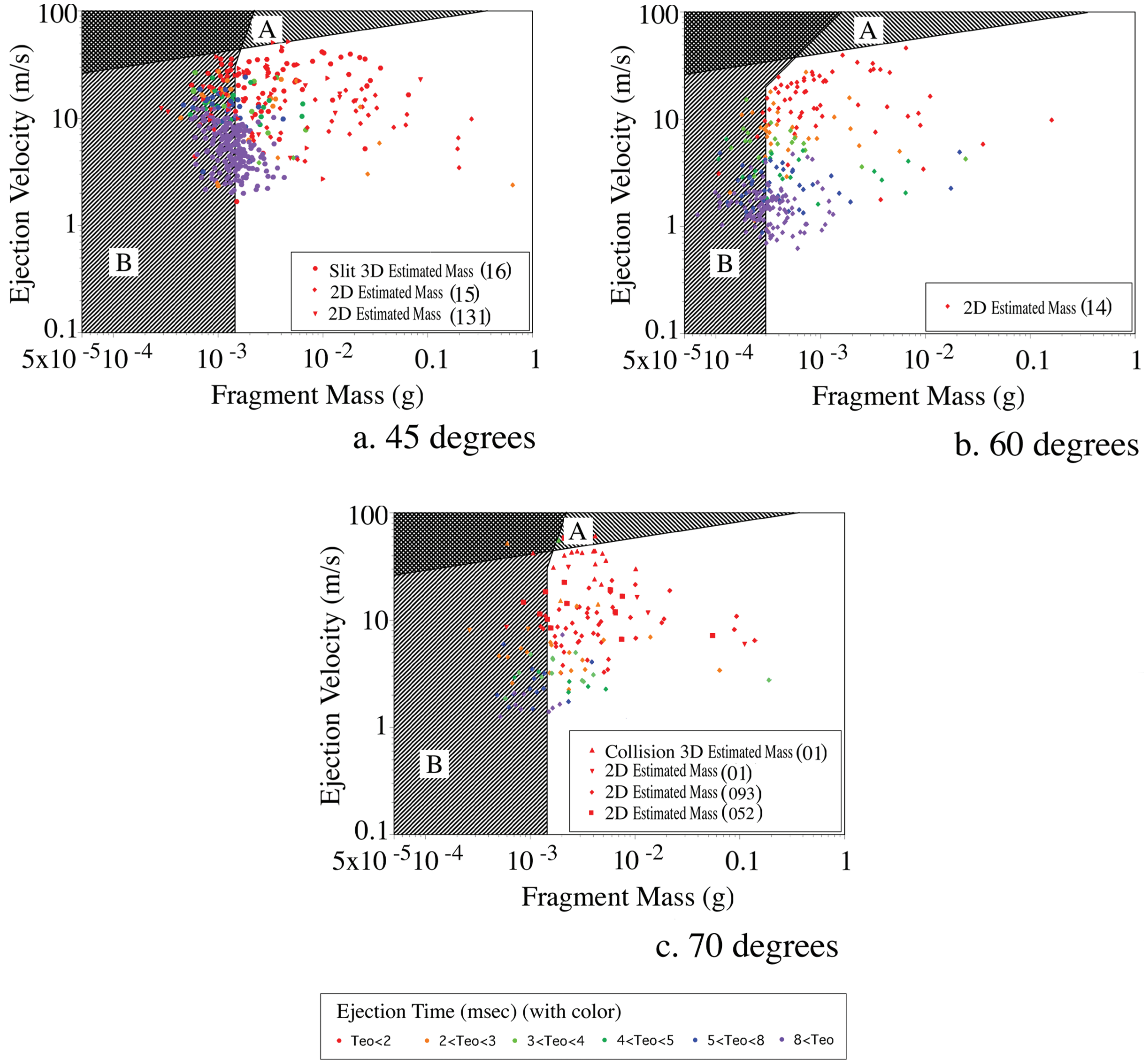

Fig. 7. Mass-velocity distributions for oblique impacts. The colors indicate different ejection times after impact, estimated from the trajectory of each fragment. The shapes represent various experiments and different ways to get fragment masses. The solid and smaller points represent the supplemented data (15, 131, 052, and 093) in which only larger or earlier fragments were observed. The hatched areas (A) and (B) represent regions where measurements are difficult because the fragments are either too small or too fast, respectively. These regions are sensitive to camera conditions like object distances, so they are different for the different experiments: a) 45° impact angle experiments, employing the target box with (experiment No. 16) and without (experiments No. 15 and No. 131) the slit. The latest fragments were not observed in the experimental run No. 16. Only early or large fragments were checked for experiments No. 15 and 131; b) 60° impact angle experiments without the slit (experiment No. 14). 2D projective velocities were measured; c) 70° impact angle experiments without the slits (experiments No. 01, No. 052, and No. 093). Late fragments were not observed as the upper surface of the target was shot.

plotting schematic as in Fig. 8. Their region I covers a size range from the largest fragments to 10^{-2}–10^{-3} times that of the target mass fragments, and their regimes II and III represent the intermediate regime and finest regime, respectively. It is possible to estimate the power-law index b in each region from:

$$N(>m) = Am^{b} \tag{3}$$

where $N(>m)$ gives the cumulative number of fragments heavier than m, and A and b are constants. Takagi et al. (1984) have shown that the slopes have positive correlations with the nondimensional impact stress, P_I in regimes I and II for the disruptive studies. They have also shown that the slopes in region III were almost constant, and they were ~0.4–0.6.

In this study, each region is justified with fragments produced by the cratering, referring to Takagi et al. (1984) as follows. First, region I consists of the ten largest fragments, and it is strongly affected by small-number statistics. Some of the plots of Fig. 8 have inflections in this region. We did not deal with this region here, both because the slopes of this region spread and because we did not vary the P_I in this study. Using all the fragments (heavy solid line), regions II and III are defined in the smaller fragment mass regions next to

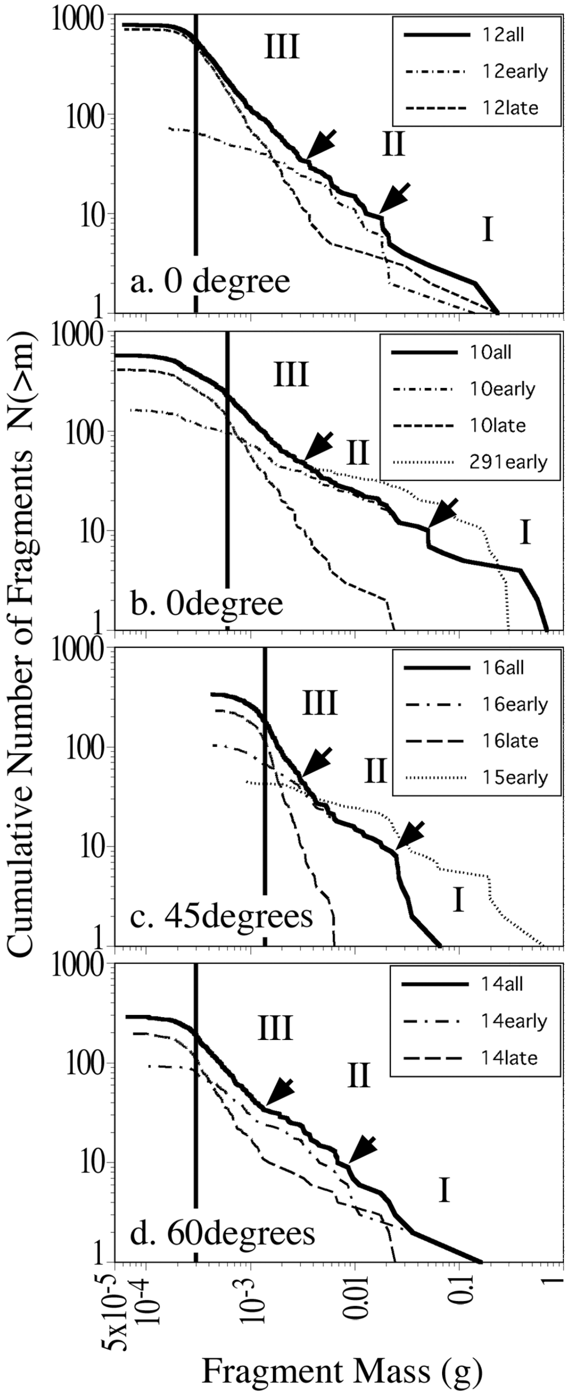

Fig. 8. Cumulative number of fragments larger than or equal to a given mass versus fragment mass distribution in impact cratering. Solid, dash-dot, and dashed lines represent mass distributions of total, early, and late fragments, respectively. The graphs show a flat region in the smallest fragment mass region displaying the lower detective limits in the fragment masses. The largest fragment means the largest fragment ejected from the crater cavity, and not the original target with a crater. Arrows indicate boundaries between regions introduced by Takagi et al. (1984), and the vertical lines show detection limits: a) 0° (No. 12); b) 0° (No. 10 and 291); c) 45° (No. 16 and 15); and d) 60° (No. 14).

region I, divided by an inflection as shown in Fig. 8. The power-law indices for each impact and each region are listed in Table 3.

The mass-cumulative number distributions for early and late populations were individually described by a power-law for each plot within each fragment mass range smaller than region I and larger than the detection limit. The cumulative number of early fragments is larger than that of late fragments for masses larger than 0.005 g. The slope for the late group is steeper than for the early group. The power law indexes were -0.49 ± 0.18 and -1.49 ± 0.09 for early and late fragments, respectively. In experiment No. 16, the resolution of the video camera was so low that the fragment mass range was not enough for curve fitting, so we excluded the data of this experiment. The power-law indices for each impact and each group are listed in Table 3.

DISCUSSIONS

The inflections in mass-cumulative number distributions can be explained by use of the early and late groups. The power law index for early fragments gives almost the same value as that in regime II. This suggests that region II is governed by the mass distribution of early fragments, since the early population consists of larger fragments more than late fragments. As the number of late fragments becomes comparable to that of early fragments, the cumulative number of total fragments shows a steep increase resulting in a knee on the mass distribution. Defining the threshold fragment mass between region II and III as that of the tenth largest fragment of the late group for each experiment corresponds with the inflection on each plot. Region III shows a slope that is intermediate between those of early and late fragments. Region IV is speculated to be the region dominated by the smallest fragments, where the total number of fragments is governed by the late fragments. The slope in region IV is steeper than that in the region III, with the same value of late fragments.

The power-law index for region II in this study is a little smaller than that for regime II in the less destructive event in Takagi et al. (1984), in which the mass of the largest fragment is larger than 30% of the original target mass. The slope in region III in this study is -1.12 ± 0.08, and it is steeper than that of previous studies (e.g., -0.4 to -0.6 in Takagi et al. [1984]; -7 to -9 in Kato et al. [1995], etc.). The data of this study indicate smaller power law indexes for the mass-cumulative number distributions, and this result may be caused by the difference in the material property of the target, the percentage of early fragments, and the analytical error associated with estimating fragment mass from their size. The fragment mass-cumulative number distribution in a catastrophic impact disruption producing the largest fragment of ~1% of the target mass in Fujiwara et al. (1977) shows a single slope of -1.4, which is close to the value for the late fragments in this work. This value of the total cumulative number may, thus, be

Table 3. Indexes of fragment mass-cumulative number distributions.

Run number	Impact Angle	All fragments			Early fragments	Late fragments
		Region I	Region II	Region III		
10	0°	−0.55	−0.55	−1.05	−0.59	−1.47
12	0°	−0.91	−0.84	−1.05	−0.46	−1.41
14	60°	−0.88	−0.72	−1.10	−0.75	−1.59
15	45°	−0.58	−0.32	n.a.	−0.31	n.a.
16	45°	−1.86	−0.95	−1.73	−0.77	−2.82
291	0°	−2.34	−0.34	n.a.	−0.35	n.a.

governed by the number of the late fragments, probably because the impact shattered early larger fragments that originated from the surface of the target into small pieces.

It seems possible to connect these two fragment groups through initial positions in the crater and relative fracture mechanisms: early fragments are mainly produced by the tensile stress reflected at the surface in a spalled region surrounding a central bowl-shaped cavity. The larger fragments among early fragments are all spall fragments, as confirmed from observation of the recovered fragments. It is also reasonable to assume that early smaller ejected fragments may be produced by spallation because of both their earlier ejection time and their initial positions estimated by their trajectory.

The late fragments are thought to be produced by a shock wave or a powerful plastic wave exceeding the Hugoniot Elastic Limit. Over 80% of these late fragments come from the bowl shaped region of the crater, and the later ejection time implies that they originate from a deeper place in the target. Bottoms and walls of the bowl shaped regions are very fragile, showing that the fragments in this cavity are produced through compressive destruction.

Figure 9 shows ejection velocity versus cumulative mass distribution of 0° vertical impact cratering on gypsum, composed of two experimental data, No. 12 and No. 10. To examine the fraction of slow fragments, fragment masses were added in ascending order. Experiment No. 12 was performed with the slit to see the cross sectional view of the ejecta flow, and therefore, the number of fragments, especially at large sizes, was reduced. On the other hand, in experiment No. 10, the analysis focused only on early and large fragments that were lacking in No. 12. Therefore, mass and velocity data from experiment No. 10 (without slit) for fragments larger than 0.008 g were used, assuming that all the fragments larger than 0.008 g were detected. Mass and velocity data from experiment No. 12 (with slit) were employed for fragments smaller than 0.008 g and allocated to ejection angle bins of 7.5° depending on their solid angle. A total ejected mass of 14 ± 1.3 g was estimated by filling the crater with glass beads. Of this, 1.4 ± 0.5 g and 0.6 ± 0.4 g were ejected with velocities slower than 2 and 1 m/s, respectively, including the second spall layer of the fragments.

There are four candidate mechanisms that can fill the blank between the ejected mass estimated from crater volume and the cumulative mass measured from the silhouette. First is vaporization of the target material. But, it is localized at the impact site. Second is fragments faster than the detection limit, like jetted material, powdery fragments flowing with the vapor cloud, and a part of conical ejection at a speed of over 100 m/s. The amount of the jetted material seems very small, as in Love et al. (1993), since the witness paper around the target suffered no impact damage within the region from 0° to 15° from the target surface. It is very hard to estimate the mass of the powder and the conical ejection. Third is fragments smaller than the detection limit. Some fragments may have been overlooked since the trajectory of the fragments overlapped. But these smaller fragments play a minor role in the cumulative mass.

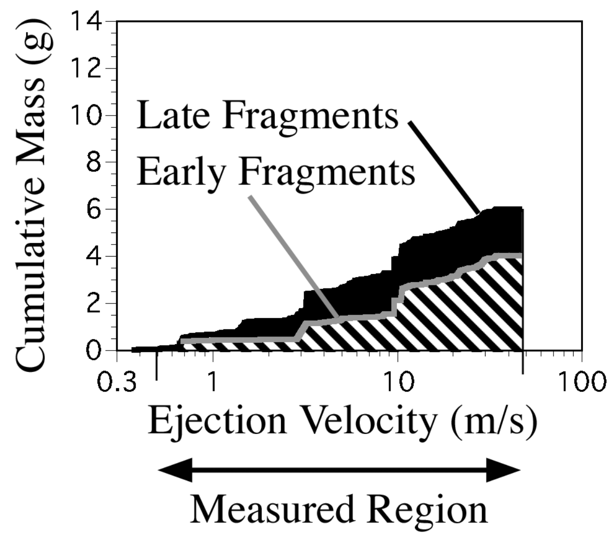

Fig. 9. Fragment velocity-cumulative mass distribution for composed run of impact angle of 0°. For the fragments larger than 0.008 g, data from experiment No. 10 were used, assuming all the fragments in this mass range could be detected. For those smaller than 0.008 g, data from experiment No. 12 were employed and allocated into elevation angle bins of 7.5° depending on their solid angle. The maximum value of the y-axis indicates the ejected mass estimated by the crater volume measured by grass beads.

The compaction of the target may contribute to the lack of mass, as is speculated for the Mathilde reference (e.g., Veverka et al. 1997; Housen et al. 1999). The ejected mass calculated by a difference in size between before and after the cratering event is significantly smaller than that estimated by filling the crater cavity with glass beads. Although the uncertainties in measurements are still large, the difference in the masses measured in two different ways is 2 g.

It is interesting to apply the velocity-cumulative mass distributions obtained in this study to small asteroids to compare ejection and escape velocities for small asteroids. The impact velocity of 4.2 km/s from our study is almost comparable to the average collisional velocity in the asteroid belt. Assuming that the effect of porosity is almost the same on gypsum targets and on asteroids, and that material differences both in projectile and target are negligible, 21 ± 7% of the fragments ejected from the crater would reaccumulate on an asteroid with density around 1500 kg/m^3 and 13 km in diameter. In the case of asteroids 4.4 and 2.2 km in diameter, 10 ± 3% and 4 ± 3% of the fragments ejected from the crater will reaccumulate, although the uncertainty is still large. This exercise suggests that an Eros-sized porous asteroid should have a regolith produced by impact cratering. In the case of a porous asteroid smaller than 2 km in diameter, however, the deposition ratio seems to be small.

CONCLUSIONS

Impact cratering experiments on gypsum target were performed, and fragments' mass and velocity were measured by the use of high-speed video cameras. Fragments ejected in impact cratering can be divided into two groups: early and late fragments. The mass-velocity distribution indices for early fragments ranges between −0.11 and −0.07. More than 80% of late fragments appear in the low velocity and small size region, i.e., 0.86 to 8.6 m/s in velocity and 0.0002–0.0016 g in mass. When the impact angle varies from vertical to 60°, the averaged ejection angle of late fragments varies from 90° to 76° from the target surface. The mass distribution consists of two different slopes: −0.49 ± 0.18 for early fragments and −1.5 ± 0.1 for late fragments. Applying the velocity-mass distributions obtained in this study to small asteroids, in the cases of asteroids 4.4 km and 2.2 km in diameter, 10 ± 3% and 4 ± 3% of the fragments ejected from the crater will reaccumulate.

Acknowledgments–The authors thank Drs. E. Asphaug, S. G. Love, and E. Pierazzo for their constructive and insightful reviews. Their comments greatly improved this paper. We acknowledge Drs. Kato and Yamori for their kind assistance and useful discussions. We thank Dr. Nakazawa, Dr. Hasegawa, and Ms. Okudaira for their help with the experiments. Discussions at the Impact Cratering Workshop in February 2003 were helpful, and we thank Dr. Herrick and Dr. Pierazzo for the meeting.

Editorial Handling—Dr. E. Pierazzo and Dr. R. Herrick

REFERENCES

Britt D. T., Yeomans D., Housen K., and Consolmagno G. 2002. Asteroid density, porosity, and structure. In *Asteroids III,* edited by Bottke W. F., Cellino A., Paolicchi P., and Binzel R. P. Tucson: University of Arizona Press. pp. 485–500.

Chapman C. R., Merline W. J., Thomas P. C., Joseph J., Cheng A. F., and Izenberg N. 2002. Impact history of Eros: Craters and boulders. *Icarus* 155:104–118.

Fujiwara A., Kamimoto G., and Tsukamoto A. 1977. Destruction of basaltic bodies by high-velocity impact. *Icarus* 31:277–288.

Fujiwara A., Kamimoto G., and Tsukamoto A. 1978. Expected shape distribution of asteroids obtained from laboratory impact experiments. *Nature* 272: 602–603.

Gault D. E. and Heitowit E. D. 1963. The partition of energy for hypervelocity impact craters formed in rock. Proceedings, 6th Hypervelocity Impact Symposium. pp. 419–456.

Gault D. E., Shoemaker E. M., and Moor H. J. 1963. Spray ejected from the lunar surface by meteoroid impact. Technical note D-1767.

Giblin I., Martelli G., Farinella P., Paolicchi P., Di Martino M., and Smith P. N. 1998. The properties of fragments from catastrophic disruption events. *Icarus* 134:77–112.

Housen K. R., Holsapple K. A., and Voss M. E. 1999. Compaction as the origin of the unusual craters on the asteroid Mathilde. *Nature* 402:155–157.

Kato M., Iijima Y., Arakawa M., Okimura Y., Fujimura A., Maeno N., and Mizutani H. 1995. Ice-on-ice experiments. *Icarus* 113:423–441.

Love S. G., Hörz F., and Brownlee D. E. 1993. Target porosity effects in impact cratering and collisional disruption. *Icarus* 105:216–224.

Nakamura A. and Fujiwara A. 1991. Velocity distribution of fragments formed in a simulated collisional disruption. *Icarus* 92:132–146.

Nakamura A., Sugiyama K., and Fujiwara A. 1992. Velocity and spin of fragments from impact disruptions 1. An experimental approach to a general law between mass and velocity. *Icarus* 100: 127–135.

Polansky C. A. and Ahrens T. J. 1990. Impact spallation experiments: Fracture patterns and spall velocities. *Icarus* 87:140–155.

Shrine N. R. G., Burchell M. J., and Grey I. D. S. 2002. Velocity scaling of impact craters in water ice over the range 1–7.3 km/s. *Icarus* 155:475–485.

Simakov G. V., Pavlovsky M. N., Kalashnikov N. G., and Trunin R. F. 1974. Shock compressibility of twelve minerals. *Izvestiya Physics of the Solid Earth* 8:488–492.

Takagi Y., Mizutani H., and Kawakami S. 1984. Impact fragmentation experiments of basalts and pyrophllites. *Icarus* 59: 462–477.

Vekinis G., Ashby M. F., and Beaumont P. W. R. 1993. Plaster of Paris as a model material for brittle porous solids. *Journal of Material Science* 28:3221–3227.

Veverka J., Thomas P., Johnson T. V., and Matson D. 1986. The physical characteristics of satellite surfaces. In *Satellites,* edited by Burns J. A. and Matthews M. S. Tucson: University of Arizona Press. pp. 342–402.

Veverka J., Thomas P., Harch A., Clark B., Bell J. F., III, Carcich B., Joseph J., Chapman C., Merline W., Robinson M., Malin M., McFadden L. A., Murchie S., Hawkins S. E., III, Farquhar R., Izenberg N., and Cheng A. 1997. NEAR's flyby of 253 Mathilde: Images of a C asteroid. *Science* 278:2109–2114.

Yano H., Hasegawa S., Abe M., and Fujiwara A. 2002. Asteroidal surface sampling by the MUSES-C spacecraft. Special Paper 500. Proceedings, Asteroids, Comets, Meteors 2002. pp. 103–106.

Yeomans D. K., Antreasian P. G., Barriot J. P., Chesley S. R., Dunham D. W., Farquhar R. W., Giorgini J. D., Helfrich C. E., Konopliv A. S., McAdams J. V., Miller J. K., Owen W. M., Jr., Scheeres D. J., Thomas P. C., Veverka J., and Williams B. G. 2000. Radio science results during the near-shemaker spacecraft rendezvous with Eros. *Science* 289:2085–2087.